NUMERICAL FLUTTER ANALYSIS OF TURBOMACHINERY BLADINGS BASED ON TIME-LINEARIZED, TIME-SPECTRAL AND TIME-ACCURATE SIMULATIONS

Markus May[1], Yann Mauffrey[2], and Frédéric Sicot[2]

[1]DLR – German Aerospace Center
Institute of Aeroelasticity
Bunsenstraße 10
37073 Göttingen, Germany
markus.may@dlr.de

[2]ONERA – the French Aerospace Lab
Aeroelasticity and Structural Dynamics Department
29 avenue de la division Leclerc
92322 Châtillon Cedex, France
yann.mauffrey@onera.fr, frederic.sicot@onera.fr

Keywords: turbomachinery aeroelasticity, flutter analysis, CFD, time-linearization, harmonic balance

Abstract: Within the European research project FUTURE a transonic compressor rotor has been evaluated with respect to its aeroelastic stability. Based on the identical computational mesh different numerical approaches of the DLR flow solver TRACE and the ONERA code elsA are compared in this paper: whereas a time-linearized method based on small time-harmonic perturbations of the steady flow field is chosen in TRACE, elsA uses a non-linear time-domain harmonic balance method in order to determine local aerodynamic work entries and the corresponding global damping values for all inter-blade phase angles (IBPA).
Furthermore, nonlinear reference solutions for the critical IBPA range will be provided by both codes using their classical time-marching schemes. In this context the difference in terms of computational effort between the fast linearized or harmonic balance methods and the classical nonlinear techniques shall be highlighted as well.

1 INTRODUCTION

The European research project FUTURE – an acronym for Flutter-Free Turbomachinery Blades – aims at improving aeromechanical analysis for aggressively lightweight blade designs by advancing the state-of-the-art in flutter prediction capabilities and design rules. This will finally enable highly efficient and environmentally friendly aero engines and gas turbines. Several interconnected turbine and compressor experiments will be performed and the results will be compared with numerical simulations of the corresponding blade assemblies interfering with the surrounding flow during vibration. Therefore, all major European aero engine and stationary turbine manufacturers as well as relevant academic partners in the field of turbomachinery aeroelasticity are involved (cf. [1]).

Within the scope of one specific work package, a rotor susceptible to flutter has been designed for the one-and-a-half stage compressor rig at TU Darmstadt illustrated in Figure 1. The design-supporting predictions have been carried out by the industrial partners

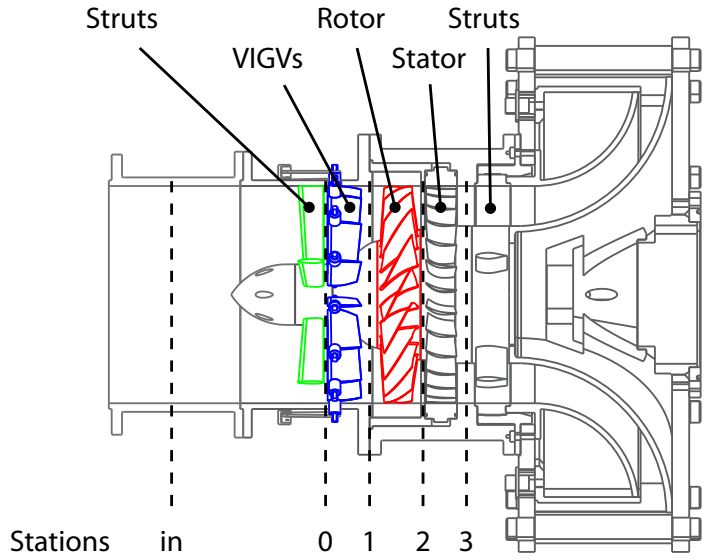

Figure 1: Cross section of the FUTURE compressor rig at TU Darmstadt

Volvo Aero Corporation, MTU Aero Engines and Siemens Industrial Turbomachinery. The design procedure as well as the corresponding results are outlined in [2]. Both of them represent the foundation this analysis is based on.

For the pre-test flutter assessment, the DLR solver TRACE as well as the ONERA code elsA were used among others to assess the aeroelastic stability of the first eigenmode of this rotor. In this context different time integration schemes are compared with respect to the unsteady pressure distribution on the blade surface.
The analysis will focus on two operating points at design speed one on the working line and the other one near the surge line. In the latter case a stronger shock will appear and flow separation might be present. Thus differences between time-linearized, time-spectral and time-accurate schemes are expected. The present study should state the performance of these methods, both in physics quality and in computational efficiency, in order to delimit their rules of good usage. The aero engine manufacturers will eventually have fast and accurate tools to help them designing flutter free turbomachinery bladings.

2 THEORETICAL CONCEPTS

2.1 Aeroelastic Modeling

The governing aeroelastic equations of motion in generalized blade coordinates $\vec{q}_i$ yield

$$\boldsymbol{M}\,\ddot{\vec{q}}_i(t) + \boldsymbol{K}\vec{q}_i(t) = \boldsymbol{\Phi}^H \vec{f}_i(t) = \vec{G}_i(t), \tag{1}$$

where $\boldsymbol{M}$ and $\boldsymbol{K}$ are generalized mass and stiffness matrix respectively. For a detailed derivation please refer to [3]. Structural damping has already been neglected in Equation (1). Since we are dealing with a modern blisk (integrally bladed rotor), hardly any mechanical damping is present and flutter susceptibilty can directly be deduced from the sign of the aerodynamic damping value.
It shall be mentioned that in this generalized modal form the equations of motion represent energy equations, where the generalized aerodynamic forces (GAF) on the right-hand

side express the work done by the motion induced unsteady aerodynamic loads in the displacements of the individual mode shapes $\vec{\phi}_i^{(r)}$ for $r = 1, 2, ..., R$.
The vector of unsteady aerodynamic forces acting on the i-th blade depends on its own blade motion as well as on its neighbors'. The time history of these movements is taken into account by the inter-blade phase angle (IBPA)

$$\sigma_n = \frac{2\pi n}{N} \quad \text{with} \quad n = 0, 1, \ldots, N-1. \tag{2}$$

This fundamental concept formulated in [4] describes a traveling wave in which all N blades are oscillating harmonically with a certain (constant) phase shift of σ_n, whereas mode shape and vibration frequency are identical.
As outlined in [5] the motion induced unsteady aerodynamic forces for the blades oscillating in the respective traveling wave modes can be expressed as

$$G_i(t) = (p_{t1} - p_1) A_0 \sum_{n=0}^{N-1} C_{\sigma_n} \hat{q}_{\sigma_n} e^{j(\omega t + i\sigma_n)}, \tag{3}$$

where $(p_{t1} - p_1)$ denotes the dynamic pressure at the entry and A_0 is the surface area of the blade. The non-dimensional complex coefficients C_{σ_n} can be deduced from the unsteady aerodynamic pressure distribution $\hat{C}_p$ on the blade oscillating with the inter-blade phase angle σ_n in the modal form $\vec{\phi}$.

2.2 Influence Coefficient Representation

The kinematic relationship between all traveling wave motions and the displacement of all blades $i = 0, 1, \ldots, N-1$ writes

$$\vec{q}_i(t) = \boldsymbol{E} \vec{\hat{q}}_{\sigma_n} e^{j\omega t}, \tag{4}$$

where $\hat{q}_{\sigma_n}$ is the amplitude of the traveling wave mode with inter-blade phase angle σ_n. The matrix elements of $\boldsymbol{E}$ are defined as $E_{i,n} = e^{j\frac{2\pi i n}{N}}$ for $i, n = 0, 1, \ldots, N-1$. Assuming a perfectly tuned system ($\boldsymbol{M} = M_0 \boldsymbol{I}$, $\boldsymbol{K} = M_0 \omega_0^2 \boldsymbol{I}$ and $\vec{\phi}_i = \vec{\phi}_0$) and introducing Equations (3,4) in (1) finally leads to the flutter stability equations in two different forms: in traveling wave coordinates

$$-\omega^2 M_0 \boldsymbol{I} \vec{\hat{q}}_{\sigma_n} + M_0 \omega_0^2 \boldsymbol{I} \vec{\hat{q}}_{\sigma_n} = (p_{t1} - p_1) A_0 \boldsymbol{C_{\sigma_n}} \vec{\hat{q}}_{\sigma_n} \tag{5}$$

as well as in blade coordinates

$$-\omega^2 M_0 \boldsymbol{I} \vec{\hat{q}}_i + M_0 \omega_0^2 \boldsymbol{I} \vec{\hat{q}}_i = (p_{t1} - p_1) A_0 \boldsymbol{L} \vec{\hat{q}}_i. \tag{6}$$

The elements of the cyclic influence coefficient matrix

$$\boldsymbol{L} = \boldsymbol{E} \boldsymbol{C_{\sigma_n}} \boldsymbol{E}^{-1} = \begin{bmatrix} L_0 & L_{N-1} & L_{N-2} & \cdots & L_1 \\ L_1 & L_0 & L_{N-1} & & L_2 \\ L_2 & L_1 & L_0 & \ddots & \vdots \\ \vdots & & \ddots & \ddots & L_{N-1} \\ L_{N-1} & L_{N-2} & \cdots & L_1 & L_0 \end{bmatrix} \tag{7}$$

denote the aerodynamic influence of a specific blade on another one. Whereas the self-influence of the reference blade (index 0) is of constant stabilizing nature, the immediate neighbors (indices 1 and $N-1$) give a harmonically varying contribution, which can be seen as first harmonic oscillation in inter-blade phase angle. Accordingly, blades arranged further away contribute with the corresponding higher harmonic variation. Numerous studies – [6] and [7] amongst others – revealed that the influence rapidly decreases with increasing distance from the reference blade and attains convergence after blade pair ± 2. However, it has been demonstrated in [8, 9] that higher influence coefficients might be present if – in the case of a throttled operating point – a strong shock is located before the leading edge of the blade.
Applications of this theory with respect to experimental setups can be found in [10, 11] who applied the transformation from influence coefficients to traveling wave modes in order to determine the aeroelastic stability behaviour of compressor and turbine cascades, respectively.

2.3 Energy Method

The classical approach for numerical flutter analysis of turbomachines is based on the energy method, described in [12], that has stood the test of time.
It assumes that the effects of aerodynamic forces on the structural dynamics properties of the aeroelastic system can be neglected, i.e. there will be no changes of mode shapes and eigenfrequencies due to unsteady aerodynamic blade loadings. Accordingly, one deals with a weakly coupled problem and can thus determine eigenmodes and natural frequencies in advance.
The prescribed motion of the blades – resulting from the respective eigenbehaviour of the rotor –, leads to unsteady airloads by means of pressure variations $\hat{p}$ on the blade surface. The global aerodynamic work per cycle W_c describes the work exerted by the fluid on a given blade within one period of its motion. In this context a positive work entry ($W_c > 0$) indicates that energy is transfered from the air flow to the structure exciting the blade. For a negative work entry ($W_c < 0$) in contrast, the blade releases energy so that oscillations are damped. The respective damping value in terms of logarithmic decrement can be deduced as

$$\Lambda = -\frac{W_c}{2E_{kin}^{max}}, \tag{8}$$

where the maximum kinetic energy is given by $E_{kin}^{max} = \frac{1}{2} M_0 \omega_0^2$ with modal mass M_0 and angular frequency ω_0 of the mode shape. Locally, the excitation of cell $\xi\eta$ with surface area $A_{\xi\eta}$ is represented by

$$\epsilon_{\xi\eta} = \frac{W_{c,\,\xi\eta}}{2E_{kin}^{max}\ A_{\xi\eta}}. \tag{9}$$

3 NUMERICAL APPROACHES

The TRACE code is developed for internal flows – especially in turbomachinery – at the DLR-Institute of Propulsion Technology (cf. [13]). It is in use at several German universities to perform steady and unsteady Reynolds-averaged Navier-Stokes (RANS) computations and represents the standard CFD tool for steady flow simulations at MTU Aero Engines in Munich.

The elsA code is the ONERA software for complex external and internal flow simulations and for multi-disciplinary applications involving aerodynamics. It is developed in close cooperation with CERFACS and applied at academic and industrial partners in France.

3.1 Nonlinear Time-Accurate Methods

The general system of conservation laws yields

$$\frac{\partial \vec{U}}{\partial t} + \frac{\partial \vec{F}_i(\vec{U})}{\partial x_i} + \vec{S}(\vec{U}) = \vec{0} \tag{10}$$

where $\vec{U}$ denotes the state vector of conservative variables, $\vec{F}_i(\vec{U}) = \vec{F}_{c_i}(\vec{U}) - \vec{F}_{v_i}(\vec{U})$ and $\vec{S}(\vec{U})$ the convective and viscous fluxes (with respect to coordinates x_i) and the source terms, respectively. To address aeroelastic problems with a moving mesh Equation (10) has to be rewritten in Arbitrary Lagrangian Eulerian (ALE) formulation before the spatial discretization in finite volumes is carried out:

$$\frac{\partial (V\vec{U})}{\partial t} + V\vec{R}(\vec{U}, \vec{x}, \dot{\vec{x}}) = \vec{0}, \tag{11}$$

where V shall indicate the cell volume that varies in time. The residual $\vec{R}$ depends on the flow variables $\vec{U}$ as well as on the grid coordinates $\vec{x}$ and velocities $\dot{\vec{x}}$ in order to account for the additional fluxes due to mesh deformation.

3.2 Time-Linearized Method in TRACE

At DLR, the first time-linearized solvers have been developed at the Institute of Aeroelasticity (cf. [14,15]). Finally, this led to an integration in the environment of the TRACE code [13] and its application to flutter analysis of modern compressors and turbines during the design process, as in [16].

Based on the assumption of small harmonic perturbations, the coordinates of the grid vertices $\vec{x}$ as well as the flow solution can be decomposed in a steady part (independant from time) and a time-dependant harmonic perturbation:

$$\vec{x}(t) = \vec{x}_0 + \Re\left(\vec{\hat{x}}(\vec{x}_0)e^{j\omega_0 t}\right) \tag{12}$$

$$\vec{U}(\vec{x}_0, t) = \vec{U}_0(\vec{x}_0) + \Re\left(\vec{\hat{U}}(\vec{x}_0)e^{j\omega_0 t}\right) \tag{13}$$

where ω_0 is again the angular frequency of the considered mode. Taking into account a linearized approximation of the nonlinear residual and introducing Equations (13) in (11) finally results in the following system of linear equations:

$$\left(j\omega_0 + \frac{\boldsymbol{\partial \vec{R}}}{\boldsymbol{\partial \vec{U}}}\right)\vec{\hat{U}} = -\left(\frac{\boldsymbol{\partial \vec{R}}}{\boldsymbol{\partial \vec{x}}}\vec{\hat{x}} + \frac{\boldsymbol{\partial \vec{R}}}{\boldsymbol{\partial \dot{\vec{x}}}} j\omega_0 \vec{\hat{x}} + j\omega_0 \frac{\hat{V}}{V_0}\vec{U}_0\right). \tag{14}$$

It shall be mentioned that the turbulence model has not been linearized; the constant eddy viscosity assumption was used instead. However, it is understood that this might

not be suitable for complex flow conditions with seperation.

Linear TRACE is implemented by means of finite differences of the nonlinear flux routines of the time-accurate solver. With respect to mesh deformation elliptic algorithms are employed to handle the displacement of the grid vertices before starting the time-linearized flow simulation in the frequency domain. From a numerical point of view, TRACE solves the resulting linear system of equations using a parallelized generalized minimal residual (GMRES) method with a symmetric successive over-relaxation (SSOR) preconditioner. As for the nonlinear simulations Giles' non-reflecting boundary conditions were stipulated for the unsteady computations.

3.3 Time-Spectral Method in elsA

The time-spectral method is dedicated to the simulation of time-periodic flows with one fundamental frequency. It casts a time-periodic unsteady RANS problem to the simultaneous resolution of $2N + 1$ coupled steady RANS problems. This odd number stands for stability reasons and allows to capture, at most, the N^{th} harmonic of the fundamental frequency. For further information please refer to [17, 18].
This means that for $N = 1$ time-spectral computations with 3 coupled instants have to be performed, which was done for the applications in this paper. Hence, the spatial domain was duplicated twice, each of the three instants reflecting a different position of the blade during one period of oscillation.

4 FUTURE COMPRESSOR STAGE

4.1 Speedlines for TU Darmstadt Rig

The computational grid for the compressor stage – including rotor and stator row – consists of roughly 1.9 million hexahedrons. Figure 2 shows the blade profile of the rotor surrounded by an O-block followed by a C-block. Several H-blocks represent inlet, passage section and exit of the row terminating with a mixing plane. A separate clearance block at the tip of the blade completes the mesh. Apart from the tip gap modeling the topology of the stator mesh is identical.

For the design shaft speed of 18.000 rpm speedlines have been computed with the two CFD codes TRACE and elsA. The steady flow at each operating point was determined using the implicit Reynolds-averaged Navier-Stokes solvers with two equation Wilcox $k\omega$ model as basis for turbulence closure. At the inlet radial profiles for total pressure, total temperature and flow angles were prescribed whereas a radial equilibrium for the static pressure at the outlet was assumed. The complete wall treatment – at hub, casing and on the blade – was done using logarithmic wall functions with values for the average dimensionless wall distance of $y^+ \approx 10$.
Figure 3 shows the total pressure ratio of the rotor versus the corrected mass flow of the stage. Two operating points at design speed have been chosen for the flutter analysis within the pre-test assessment: OP 8 on the working line and OP 9 near the surge line. For both of them Mach number distributions on the rotor at 10%, 50% and 90% span are provided in Figures 4(a)/(c) and 4(b)/(d), respectively.

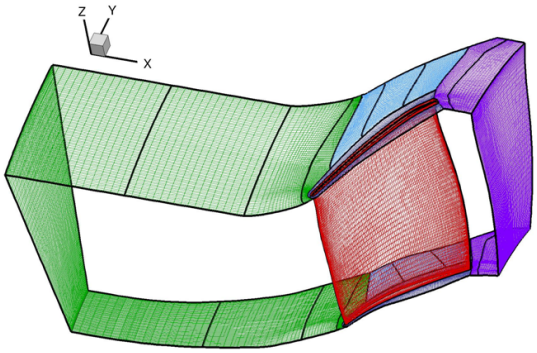

Figure 2: Block-structured mesh for rotor

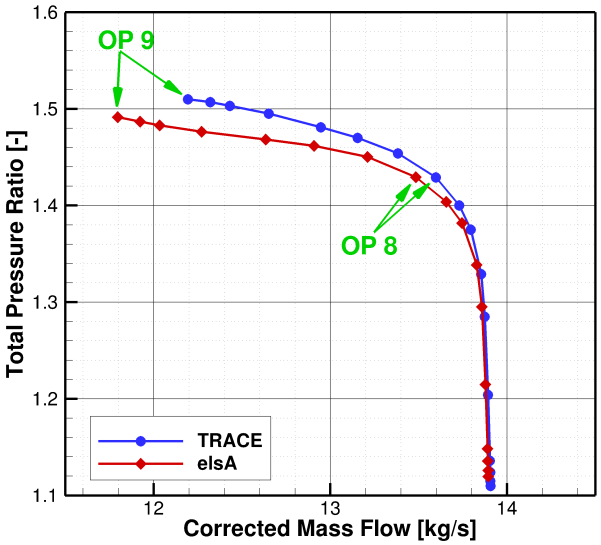

Figure 3: Rotor speedlines at 18.000 rpm

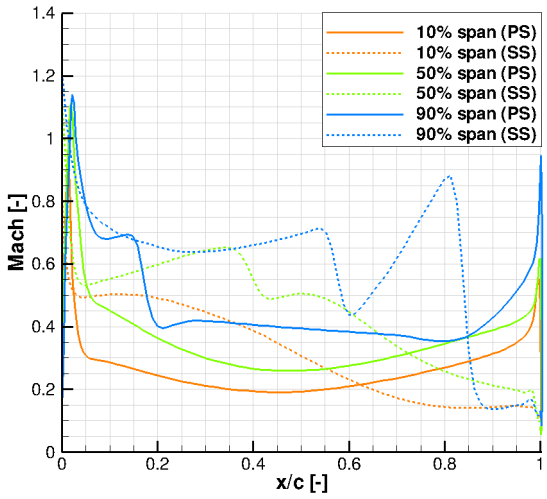

(a) TRACE at OP 8

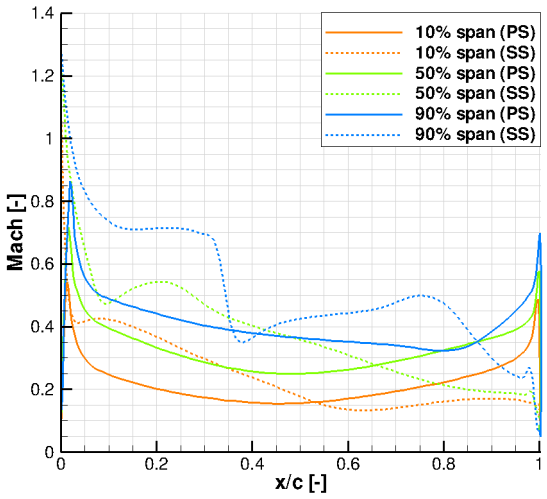

(b) TRACE at OP 9

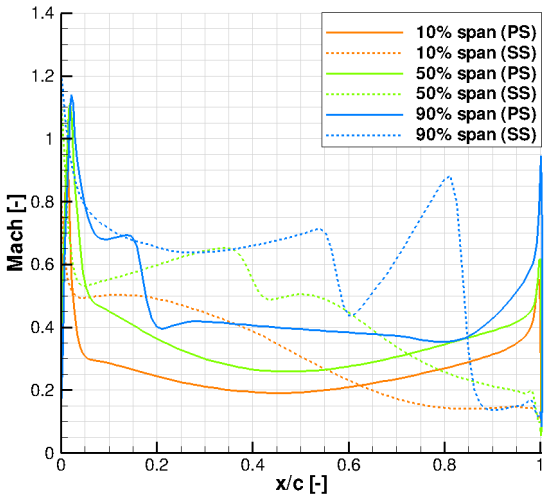

(c) elsA at OP 8

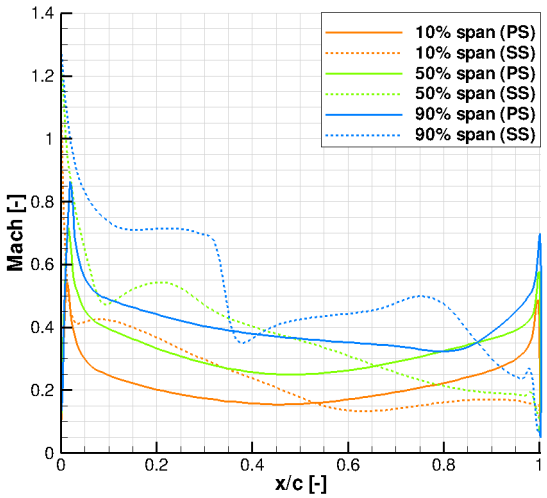

(d) elsA at OP 9

Figure 4: Steady Mach number distributions at three radial sections

Model	Nodal diameter ND [-]	Frequency f [Hz]
Blade-only	–	601.84
Blisk segment	0	591.57
	1	584.74
	2	584.98
	3	595.91
	4	597.69
	5	598.74
	6	599.48
	7	599.97
	8	600.28
	9	600.45
	10	600.54

Table 1: Eigenfrequencies of the first mode family 1F

4.2 Normal Modes Analysis

The open-source package CalculiX has been used to determine the eigenmodes of the underlying rotor. Two finite element models of the configuration are presented in Figure 5: the left-hand side shows the blade-only model whereas the influence of the disk is modeled on the right, consisting of 2782 and 5102 Hexa20 elements, respectively.
The eigenmodes of both systems have been determined for the relevant shaft speed of 18.000 rpm by means of pre-stressed normal modes analysis. The displacements for the first flex mode 1F are illustrated in Figure 6. Single point constraints as fixed support result in real mode shapes for the blade-only model. On the contrary, the blisk segment is characterized by complex mode shapes due to cyclic symmetry boundary conditions; nodal diameter (ND) 0 has been chosen for the visualization. The corresponding eigenfrequencies are documented in Table 1.

4.3 Damping Diagrams

The damping diagrams in Figure 7 show the logarithmic decrement of the aerodynamic damping for the first eigenmode family. All inter-blade phase angles have been computed with the time-linearized approach in TRACE and the time-spectral method in elsA. In addition, nonlinear reference solutions for the critical nodal diameters have been provided by both codes.

Since the imaginary part of the complex displacement in Figure 6 is five orders of magnitude smaller than its real part, no significant influence of the disk was expected for the underlying rotor. This assumption is confirmed by the comparison of blade-only and blisk model in Figure 7.
Moreover the global damping values provided by the fast time-linearized (TRACE) and time-spectral (elsA) approaches show a very good agreement with the nonlinear reference solutions for the critical IBPA range. Please note that some elsA computations are currently still missing; once the results are available they will be incorporated in an updated version of the paper.

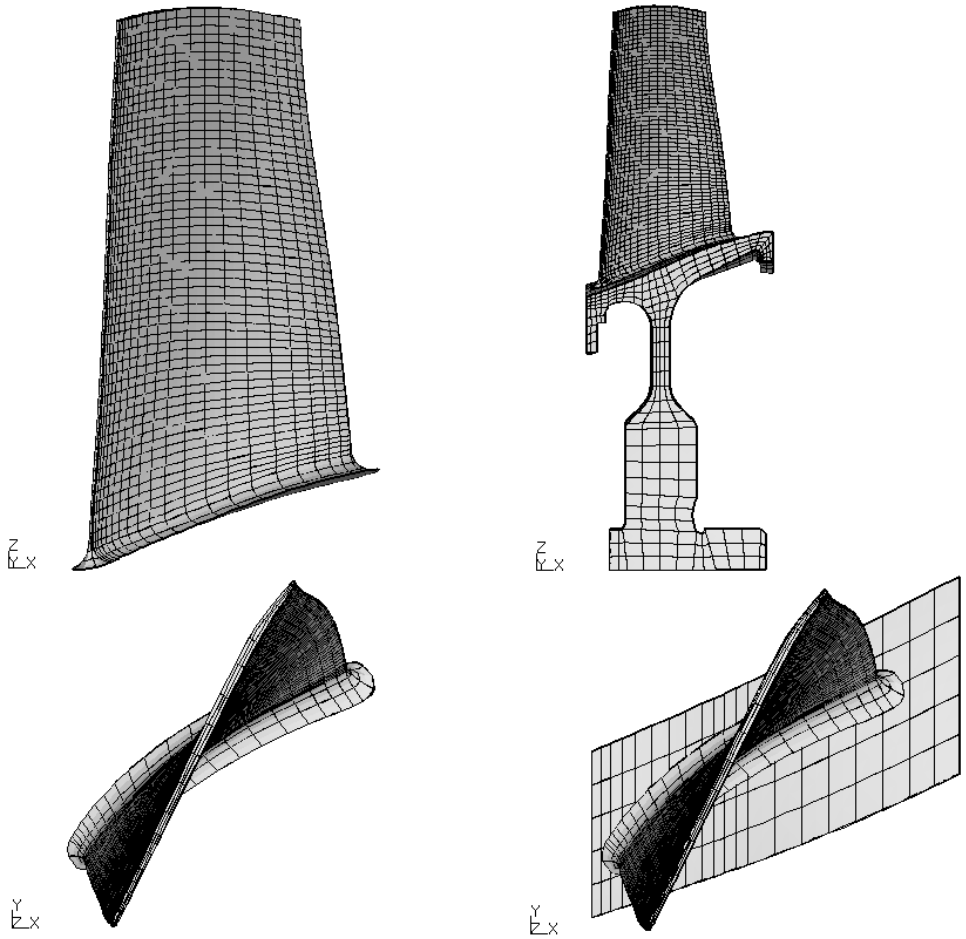

Figure 5: Finite element models: blade-only (left) and blisk segment (right)

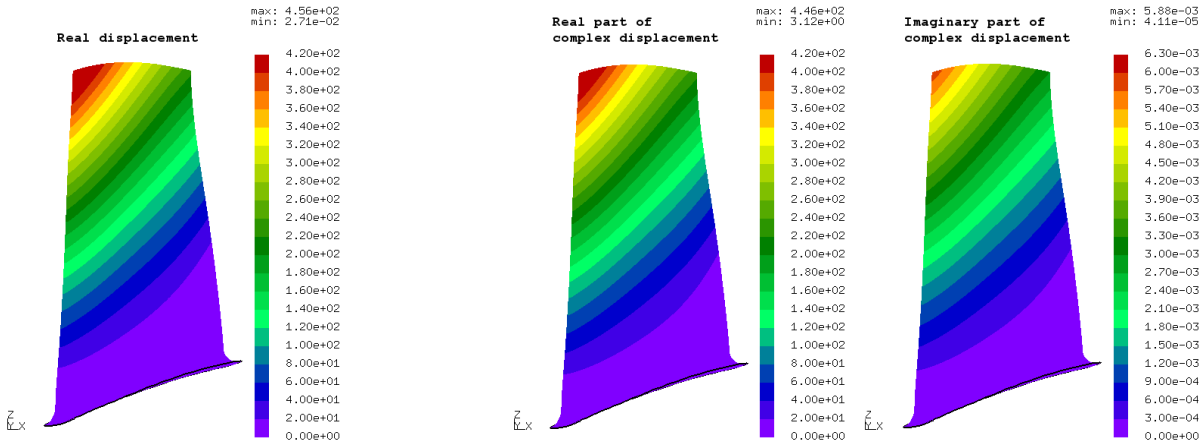

Figure 6: Displacements for eigenmode 1F of blade-only model (left) and blisk model at ND0 (right)

4.4 Local Work Entries

Figure 8 shows the local evaluation of aerodynamic force and work entries on the blade surface for the critical IBPAs of both operating points: the upper two plots show the local contribution to the generalized aerodynamic force in amplitude and phase angle; the lower plot reveals the resulting work entry. Stabilizing regions with a damping effect are marked in green whereas destabilizing areas that excite the blade are painted in red.
We can observe that the stronger shock at OP 8 has a higher stabilizing effect than its counterpart at OP 9 (cf. Figures 8(a) and (b)), leading to a higher global damping value in Figure 7(a) compared to (b).

4.5 Influence Coefficients

The influence coefficients for the eigenmode family 1 can directly be deduced – according to Equation (7) – from the generalized aerodynamic forces of the travelling wave CFD simulations.
The vectors to these points in Figure 9 are rotated in the complex plane with respect to the IBPA in order to determine the resulting stabilizing ($\Im < 0$) or destabilizing ($\Im > 0$) contribution. Only L_0 stays at its original position and thus the self-influence of a vibrating blade always has a stabilizing effect on the rotor. Considering the magnitude of L_0 compared to the other coefficients with a significant contribution – L_1 in direction of the suction side and L_{20} in direction of the pressure side –, one can easily deduce that the blisk will be stable for all inter-blade phase angles.

5 CONCLUSIONS

The unsteady results produced by the flow solvers TRACE and elsA are in very good agreement. In terms of computational efficiency especially the time-linearized and time-spectral simulations highlight the capability of these methods to adequately predict aeroelastic stability in turbomachines. Yet it has to be mentioned that this benefit will get lost once we have to deal with flow separation at the rotor. This was not the case for the present configuration as the flow around the stator separated first during throttling.

According to TRACE and elsA the FUTURE compressor setup is stable from an aeroelastic point of view at 18.000 rpm. However, further operating points (e.g. off-design conditions, different settings of variable inlet guide vanes) have been investigated during the pre-test assessment. In this context, some partners had more "promising" results with respect to flutter susceptibility. Nevertheless, the mistuning characteristics of the blisk due to manufacturing and instrumentation will probably have a strong stabilizing effect. For this reason the excitation system described in [19] has been developed, so that unsteady pressure distributions on the oscillating blades can be measured even if no free-flutter will be encountered in the experiment.

6 ACKNOWLEDGEMENTS

The authors would like to thank their FUTURE project partners for the permission to publish these results. Beyond that, the support of this work by the European Commission is gratefully acknowledged.

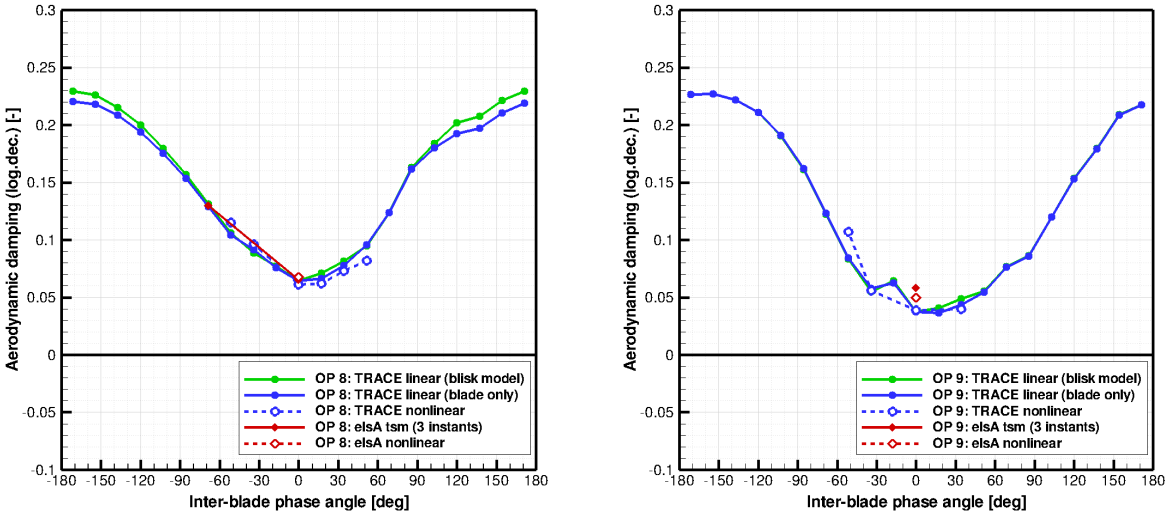

(a) Damping diagram for OP 8 (b) Damping diagram for OP 9

Figure 7: Comparison of unsteady TRACE and elsA results for the first eigenmode family

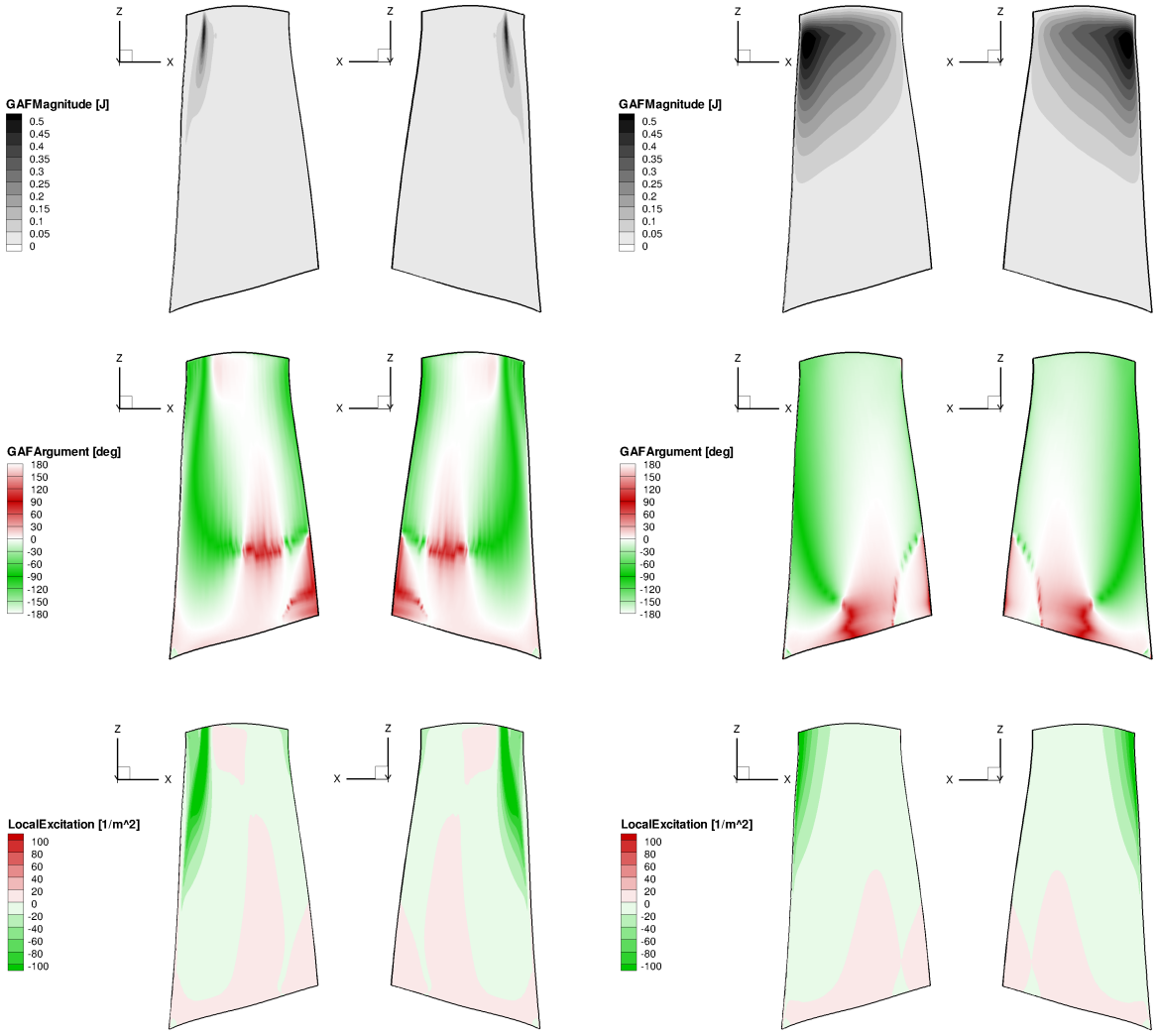

(a) OP 8: Mode 1 at $\sigma_0 = 0°$ (b) OP 9: Mode 1 at $\sigma_1 = 17.14°$

Figure 8: Local evaluation of aerodynamic force and excitation on the blade surface

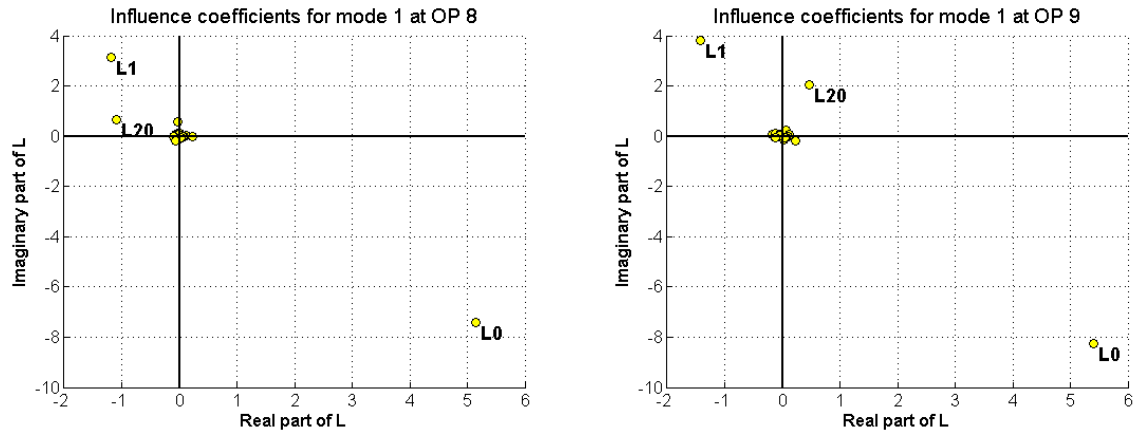

Figure 9: Influence coefficient representations in the complex plane

7 REFERENCES

[1] Website of the FUTURE Project: http://www.future-project.eu.

[2] Mårtensson, H. E., Östlund, J., Bladh, R., et al. (2011). Design and analysis of a transonic flutter research compressor. Submitted for 15th International Forum on Aeroelasticity and Structural Dynamics in Paris.

[3] Platzer, M. and Carta, F. (Eds.) (1987/88). *Aeroelasticity in Axial-Flow Turbomachines*, vol. Volume 1: Unsteady Turbomachinery Aerodynamics. Volume 2: Structural Dynamics and Aeroelasticity of *AGARDograph No. 298*. AGARD.

[4] Lane, F. (1956). System Mode Shapes in the Flutter of Compressor Blade Rows. *Journal of Aeronautical Sciences*, 23, 54–66.

[5] Kemme, R. (2004). *Numerical Investigation of the Aeroelastic Stability Behaviour of a Highly Loaded Compressor Rotor*. Ph.D. thesis, TU Hannover, Germany.

[6] Hanamura, Y., Tanaka, H., and Yamaguchi, Y. (1980). A Simplified Method to Measure Unsteady Forces Acting on the Vibrating Blades in Cascade. *Bulletin of JSME*, 23(180), 880–887.

[7] Carta, F. and St.Hilaire, A. (1980). Effect of Interblade Phase Angle and Incidence Angle on Cascade Pitching Stability. *ASME Journal of Engineering for Gas Turbines and Power*, 102, 391–396.

[8] May, M. (2011). Implementation of an Aeroelastic Tool to Deduce Influence Coefficients. Tech. Rep. IB 232 - 2011 C 05, DLR German Aerospace Center – Institute of Aeroelasticity, Göttingen, Germany.

[9] May, M. and Grüber, B. (2011). Reliability of Time-Linearized Flutter Predictions near the Surge Line. In *Proceedings of 9th European Conference on Turbomachinery Fluid Dynamics and Thermodynamics in Istanbul, Turkey*. Paper No. ETC9-2011-208.

[10] Hennings, H. (1997). *Experimental flutter investigations of a straight two-dimensional compressor cascade in incompressible flow*. Ph.D. thesis, RWTH Aachen, Germany.

[11] Vogt, D. (2005). *Experimental Investigation of Three-Dimensional Mechanisms in Low-Pressure Turbine Flutter*. Ph.D. thesis, KTH Stockholm, Sweden.

[12] Carta, F. (1967). Coupled Blade-Disk-Shroud Flutter Instabilities in Turbojet Engine. *Journal of Engineering for Power*, 419–426.

[13] Kersken, H.-P., Frey, C., Voigt, C., et al. (2010). Time-Linearized and Time-Accurate 3D RANS Methods for Aeroelastic Analysis in Turbomachinery. In *Proceedings of ASME Turbo Expo 2010 in Glasgow, UK*. Paper No. GT2010-22940.

[14] Hagenah, B. (2004). *Development and Application of a time-linearized 2D Euler Solver for Flutter Investigations in Turbomachines*. Ph.D. thesis, RWTH Aachen, Germany.

[15] Petrie-Repar, P. (2006). Development of an Efficient and Robust Linearised Navier-Stokes Flow Solver. In J. T. K.C. Hall, R.E. Kielb (Ed.), *Unsteady Aerodynamics, Aeroacoustics and Aeroelasticity of Turbomachines*, vol. VI. Springer, pp. 437–448.

[16] May, M. (2010). Sensitivity Analysis with respect to Flutter-Free Design of Compressor Blades. In *Proceedings of ASME Turbo Expo 2010 in Glasgow, UK*. Paper No. GT2010-23557.

[17] Dufour, G., Sicot, F., Puigt, G., et al. (2010). Contrasting the Harmonic Balance and Linearized Methods for Oscillating Flap Simulations. *AIAA Journal*, 48(4), 788–797.

[18] Sicot, F., Dufour, G., and Dugeai, A. (2011). A Harmonic Balance Method for Aerodynamic Damping Prediction in Turbomachinery. In *Proceedings of 9th European Conference on Turbomachinery Fluid Dynamics and Thermodynamics in Istanbul, Turkey*. Paper No. ETC9-2011-038.

[19] Holzinger, F., Biela, C., Schiffer, H.-P., et al. (2009). Development of an Excitation System for Forced Response Investigations in the TU Darmstadt Compressor. In *Proceedings of the 12th International Symposium of Unsteady Aerodynamics, Aeroacoustics and Aeroelasticiy in Turbomachines in London, UK*.